RESEARCH ARTICLE | SEPTEMBER 11 2024

On the active flow control in maglev train safety under crosswinds: Analysis of leeward suction and blowing action

Special Collection: Flow and Civil Structures

Zi-Jian Guo (郭子健); Zhan-Hao Guo (郭展豪); Zheng-Wei Chen (陈争卫) ; Guang-Zhi Zeng (曾广志); Jun-Qi Xu (徐俊起)

Physics of Fluids 36, 095130 (2024)
https://doi.org/10.1063/5.0224211

Physics of Fluids ARTICLE pubs.aip.org/aip/pof

On the active flow control in maglev train safety under crosswinds: Analysis of leeward suction and blowing action

Cite as: Phys. Fluids **36**, 095130 (2024); doi: 10.1063/5.0224211
Submitted: 20 June 2024 · Accepted: 22 August 2024 ·
Published Online: 11 September 2024

Zi-Jian Guo (郭子健),[1] Zhan-Hao Guo (郭展豪),[1] Zheng-Wei Chen (陈争卫),[1,a)] Guang-Zhi Zeng (曾广志),[1] and Jun-Qi Xu (徐俊起)[2]

AFFILIATIONS

[1]Department of Civil and Environmental Engineering, The Hong Kong Polytechnic University, Hong Kong, China
[2]National Maglev Transportation Engineering R&D Center, Tongji University, Shanghai, China

Note: This paper is part of the special topic, Flow and Civil Structures.
[a)]**Author to whom correspondence should be addressed:** zhengwei.chen@polyu.edu.hk

ABSTRACT

The design speed of high-speed maglev trains is much higher than that of wheel-rail trains, and they will be subject to more operational safety threats under complex wind conditions. The present study uses the improved delayed detached eddy simulation method based on the shear stress transfer k–ω turbulence model to explore the effect of active flow control on the aerodynamic lateral force of a maglev train and examines the main aerodynamic performance differences caused by two active control forms (suction and blowing airflow), involving multiple active flow speeds. In the current scenario, blowing can reduce the lateral force coefficient of the head car by up to 15% while greatly increasing its transient instability, which can be attributed to direct and indirect changes in pressure distribution near the air slots and a larger range of the leeward surface. The suction is believed to suppress the downstream motion of the main vortex on the leeward side of the maglev train and weaken the turbulent kinetic energy of the wake, while the blowing effect reduces the dominance of the main vortex. The application of blowing is proved as an effective means of reducing the risk of operating a maglev train in a crosswind environment, while it requires a careful consideration of both train safety and energy efficiency.

I. INTRODUCTION

Maglev trains are exempt from wheel-rail adhesion limitations to further breakthrough operating speeds and are becoming one of the options for the next generation of high-speed rail transit due to the advantages of fast start/stop, low noise, low vibration, low maintenance, and environmental friendliness.[1,2] Some maglev train lines are already in operation, such as Shanghai Maglev, Changsha Maglev, Beijing Line S1 and Fenghuang Maglev in China, Linimo (Tobu Kyuryo Line) in Japan, and Daejeon Expo Maglev and Incheon Airport Maglev in South Korea. In addition, many maglev train routes are being considered and planned in various countries, such as Sydney to Wollongong in Australia, Mumbai to Delhi in India, London to Glasgow in UK, Washington, DC to New York City in US, and Beijing to Guangzhou and Shanghai to Hangzhou in China. In view of the increasing number of maglev trains operating in the foreseeable future, the aerodynamics of maglev trains has been a subject of much scholarly attention.[3–6]

Maglev trains will face more severe aerodynamic problems due to higher expected speeds and enhanced interaction with the surrounding air, especially suffering the crosswind.[7–10] A great deal of research has been carried out to mitigate the risk of train overturning in crosswinds:[11–15] For the vehicle body itself, optimizing the aerodynamic design of the train,[16–19] improving the structure of components such as bogies and pantographs,[20–22] non-smoothing surface treatment, and installing additional aerodynamic auxiliary components[23] have been used to improve the flow behaviors of the train in crosswind environments. For trackside wind protection, windbreaks are the most widely used facility in railways.[24–27]

However, with the further increase in train speed and the more frequent occurrence of bad weather, the non-stability of train operation under crosswind conditions continues to increase. The expected operating speed of maglev trains is much higher than that of wheel-rail trains, and their unique contactless suspension makes them more susceptible to instability caused by crosswinds.[28–30] Active flow control, as

an effective means to solve the purpose of vehicle lift increase, drag reduction or stabilization, and control in aerospace field,[31,32] is also one of the potential ways that can enhance the aerodynamic performance of train in crosswinds. There have been several studies demonstrating the good application of active flow control on high-speed trains.[33–35] There have also been some preliminary studies that have considered attempts to apply active flow control methods to increase the stability of trains under crosswinds. Chen *et al.*[36] studied the effect of air-blowing on the lateral aerodynamic force experienced by trains and achieved a significant reduction in the lateral rolling moment for the cars. Guo *et al.*[37] found that active air-blowing reduces the lateral forces of a train by 1.0%–8.8% over the range of yaw angles studied. However, there is insufficient research on the coupling interaction mechanisms between active flow and airflow around the train, hindering the translation of these scientifically discovered active control strategies into engineering improvements.

Due to the different train-guideway relationship with conventional wheel-rail trains, it may produce aerodynamic performance different from that of well-studied high-speed trains under a same crosswind environment. It is unclear how effective this type of active flow control would be on a maglev train. In addition, suction can also change the airflow path over the roof of the train just like blowing, while this mixing mode with the leeward side vortex has not been studied. Building upon previous work, the current study aims to explore the ability to improve the stability of maglev trains under crosswinds through active flow control applied to the air-slots on the leeward side of the maglev train and examines the two methods of air blowing and sucking as well as their flows.

II. RESEARCH METHODOLOGY

A. Geometry model and computational domain

In this study, numerical simulations are carried out using a 1/20th scaled three-car TR08 Maglev train model to explore the effect of the proposed active flow control strategy on individual vehicles. As shown in Fig. 1(a), the flat bottom surface of the maglev body above the guideway is set as the reference plane Z = 0, and the center of the guideway is set as the reference plane Y = 0. The height H of the maglev train model from the roof to the lowermost point of the holding arms is 0.2 m, which is used as an eigenvalue to dimensionless the other dimensions. As shown in Fig. 1(b), the lengths of the head, middle, and tail cars are 6.775H, 6.375H, and 6.775H, respectively, which gives the full length of the maglev train of 19.925H. The height of the whole guideway pedestal is 0.6H, which is in line with that in the operating maglev train transport system. The air-slots with a width of 0.1H are designed on the leeward side of the maglev train, equal in length to the equal cross section segments of each car, which is 5.5H and 6.375H for the head car (same as the tail car) and the middle car, respectively. Based on the pressure distribution characteristics of the train leeward-side,[38,39] the air-slots are designed in the region where a strong negative pressure is expected to be distributed in the present running scenario, and the bottom of the slots is located at 0.65H from the lowermost point of the maglev train.

The dimensions of the computational domain and the boundary conditions are specified as shown in Fig. 2. To ensure the stability of the inlet flow, the distance from the front inlet to the nose of the maglev train is 25H. Similarly, a distance of 8H is applied between the center plane of the guideway and the side front to ensure the enough development of the incoming flow with Y-direction velocity component referring to the crosswind. In addition, to ensure that the flow develops sufficiently around the train and to minimize the influence of the boundaries on the numerical simulation, the distance from the tail of the maglev train to the back exit is 40H, and the distance from the center plane of the guideway to the side back is 16H. The height of the computational domain is 10H, where the distance from the top plane of the guideway to the bottom of the computational domain is 4H to replicate the scenario of the maglev train operating at a certain height.

Both the longitudinal and transverse inlets are designated as velocity inlet boundaries whose components are determined by the yaw angle of interest in the current study (15°). Based on the specified resultant velocity $U = 60$ m/s, the components along the X and Y directions emitted by the two velocity inlets are 57.96 and 15.53 m/s, and the Reynolds number for the numerical simulation is 7.9×10^5. A turbulence intensity of 0.05 is set in the numerical simulations, which is derived from the commonly used level in train aerodynamics.[40–42] The longitudinal and transverse outlets are configured as zero-pressure exits. The ground and guideway are set as moving no-slip wall surfaces that move at the opposite speed to the train operating speed to simulate the relative motion between the maglev train and the guideway and ground. The top surface of the computational domain is defined as a symmetric wall. The boundary conditions for all blowing slots are set as velocity inlet boundary conditions, and the blowing and sucking functions can be realized by changing the direction of the velocity.

B. Numerical scheme

The Improved Delayed Detached Eddy Simulation (IDDES) method, based on the Shear Stress Transport (SST) k–ω turbulence model, was widely used in previous studies[12,43–45] and employed to simulate the flow field characteristics of a maglev train running under crosswind conditions. The convective terms are obtained by mixing second-order windward and bounded-center differences, with a windward mixing factor of 0.15, and second-order precision is used to handle the time discretization. All three models are based on the semi-implicit method for pressure linked equations (SIMPLE) implicit scheme to solve separate flows. The time step (Δt) was set to 5×10^{-5} s to maintain a Courant number (CFL) of no more than 1. The transient simulation was performed for a total of 1 s, allowing the flow to completely

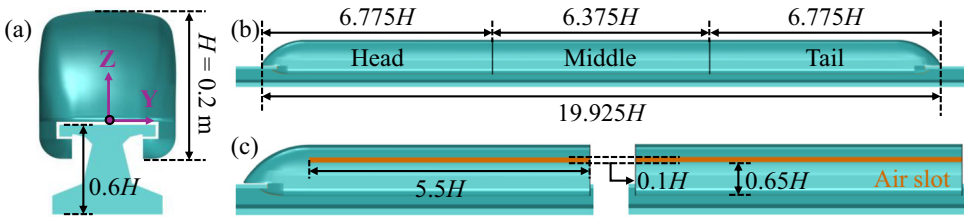

FIG. 1. Geometric model: (a) front view of the maglev train and guideway, (b) side view of the train and guideway, and (c) zoomed details of air-blowing slots in head car and middle car.

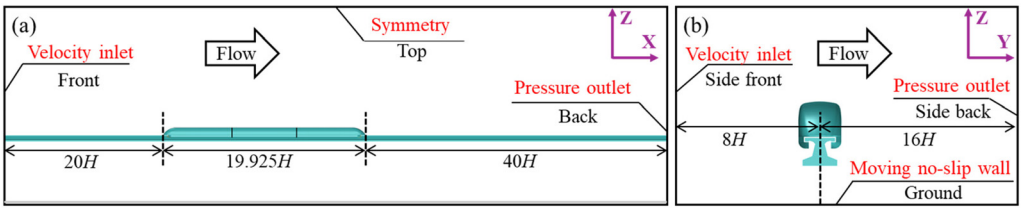

FIG. 2. Calculation domain and boundary conditions: (a) side view and (b) front view (not in scale).

pass through the slanted-base cylinder more than 15 times. A total of 20 000 steps of transient calculation and 10 000 steps of time-averaged processing were performed to ensure the complete development of the flow field and the accuracy of the time-averaged results.

C. Meshing strategy

The maglev train surface, guideway surface, and space within the computational domain are discretized using polyhedral cells for better results. From the core area that this study focuses on to the boundaries of the computational domain, four different volume control levels are used to continuously reduce the density of cells, thereby maximizing computational efficiency, see "fine," "medium," and "coarse" labels in Figs. 3(a) and 3(b). As shown in Fig. 3(c), a 15-layer prism grid with a growth rate of 1.15 is attached to the maglev train surface to accurately capture the velocity gradient in the near-wall area, thereby obtaining more reliable aerodynamic force and moment prediction. The thickness of the first prism layer is set according to the requirement of dimensionless wall distance $y^+ < 5$ and combined with the full y^+ wall treatment in STAR CCM+,[37] the current discretization strategy can meet the requirements of the turbulence model introduced in Sec. II B. The surface grid distribution on the maglev train and guideway can be seen in Fig. 3(d). The guideway surface is subjected to 10 prism layers with three or four mesh layers transitioning to the prism layers on the train surface, which allows the gap flow to be accurately resolved by nearly 30 layers of mesh.

D. Numerical method verification

The independence of the computational grid is determined using the calculation results of three sets of mesh differently discretized. Based on the differentiation of the surface grid size of the maglev train, the prism layer configuration, and the spatial volume control level of the computational domain, three sets of computational grids called fine, medium, and coarse are generated and used for independence testing. Figure 4(a) shows the lateral force coefficient Cs of the three cars predicted by these three meshes when the active airflow blows at a speed of $v_a = 0.2U$. Figure 4(b) presents the pressure coefficient Cp along the upper part of the $Y = 0$ profile of the train to show more detailed differences caused by the meshes. The two dimensionless coefficients used in this comparison, the lateral force coefficient Cs and the pressure coefficient Cp, are defined as

$$Cs = \frac{Fs}{\frac{1}{2}\rho U^2 A}, \tag{1}$$

$$Cp = \frac{P - P_0}{\frac{1}{2}\rho U^2}, \tag{2}$$

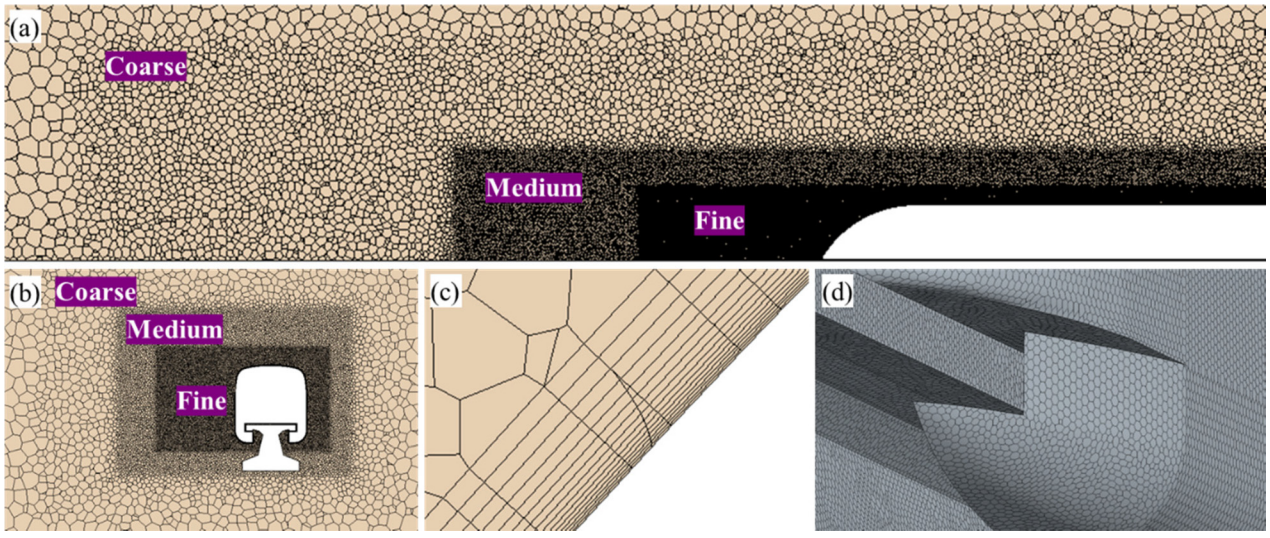

FIG. 3. The distribution of the cells on the (a) Y-slice of the domain, (b) X-slice of the domain, (c) prism layers attaching the maglev train surface, and (d) surface of maglev train and guideway.

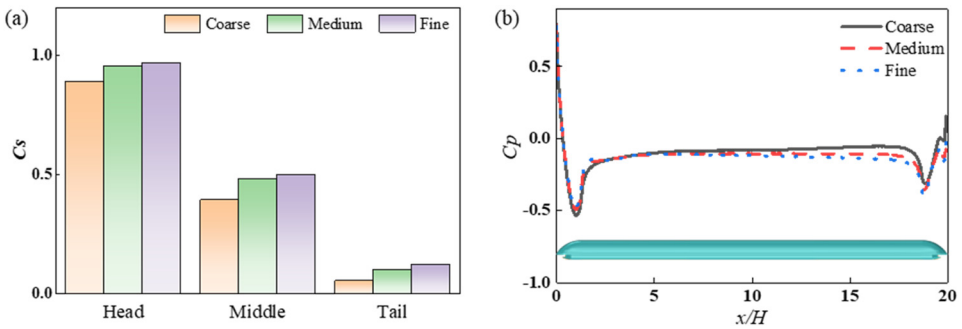

FIG. 4. The comparison of the results from three meshing in terms of (a) *Cs* of each car and (b) C_p of Y = 0 profile along the upper surface of the maglev train.

where the relative pressure P-P_0 and the lateral force *Fs* can be outputted by the solver; the air density $\rho = 1.225\,\mathrm{kg/m^3}$ was applied; the reference area *A* measures $0.0293\,\mathrm{m^2}$ for the present scaled model. The coarse mesh proved to be more different than the medium and fine meshes, which can be seen in the lower lateral force coefficient in Fig. 4(a) and the higher local negative pressure in Fig. 4(b). However, the fine mesh does not produce significantly different calculation results than the medium mesh, proving that the discretization level of the medium mesh is sufficient.

A wind tunnel test for maglev train conducted in the Hong Kong Polytechnic University is used to validate the numerical methods in the present study. As presented in Fig. 5(a), the closed-loop wind tunnel has a test section of $2.4 \times 0.6 \times 0.6\,\mathrm{m^3}$ and allows a wind speed of up to 50 m/s. As shown in Fig. 5(b), a maglev train with a scaling ratio of 1:40 is placed in the test section, and the simulation of yaw angle from 0° to 20° can be realized through the rotating slots on the bottom wall of the test section, and the blockage ratio is 3.85% when the yaw angle is 20°, without correcting the test results. A series of wind tunnel tests of a maglev train in crosswinds were carried out, in which the test speed of 15 m/s and yaw angles of 0° and 15° were replicated by numerical simulations. As in Fig. 4(b), the *Cp* distribution of Y = 0 profile along the upper surface of the maglev train is used to compare the ability of the numerical simulations to resolve the surface pressure of the maglev train for these two operating conditions. It is found in Fig. 6 that the predictions obtained by the current numerical methodology are generally in good agreement with the test results, and although there is the expected difficulty of re-prediction due to flow separation on the streamlined shoulder of the tail car, the numerical methodology can be considered sufficiently reliable to capture the flow characteristics around the maglev train.

III. RESULTS AND ANALYSIS

A. Aerodynamic lateral force

Figure 7 depicts the aerodynamic lateral force coefficients acting on the head, middle, and tail cars of a maglev train when exposed to a crosswind with a yaw angle of 15°. The impact of various active control strategies applied to the leeward side air slots is analyzed, demonstrating how suction and blowing influence the lateral forces on each car. For the head car, airflow over its streamlined structure maintains consistent initial characteristics before reaching the air slot, leading to a direct and monotonous relationship between the blowing strategy and the value of *Cs*. Specifically, suction significantly increases the lateral force coefficient, whereas blowing reduces it by up to 15% for the head car. The tail car exhibits a different pattern: a lower suction velocity causes a more substantial increase in lateral force, and the force's reduction is less affected by the intensity of blowing. This difference is attributed to the altered airflow caused by the preceding air slots and the fact that flow separation and large-scale vortices around the lead car occur outside the effective range of the air slots' active control. Conversely, for the tail car, separation happens after the air slots, rendering it unaffected by active control. The middle car responds uniquely to the active control strategies: both suction and blowing increase the lateral force it experiences, with the effect intensifying at higher active velocities. This phenomenon is linked to the surface pressure distribution on the middle car, a topic that will be explored in detail in the following sections.

Figure 8, which uses the head car as an example, illustrates the transient characteristics of lateral force coefficient *Cs* throughout the time-discrete process. It shows the distribution of lateral force coefficients and their fluctuations gradient over time. The conditions

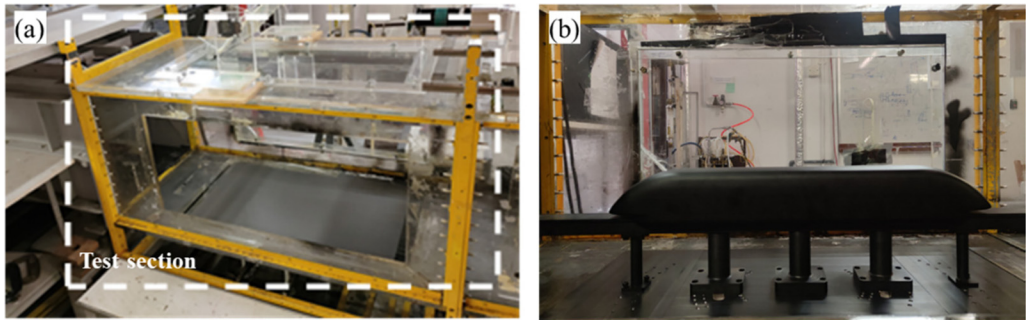

FIG. 5. The wind tunnel test in Hong Kong Polytechnic University: (a) test section and (b) maglev train model in the test section.

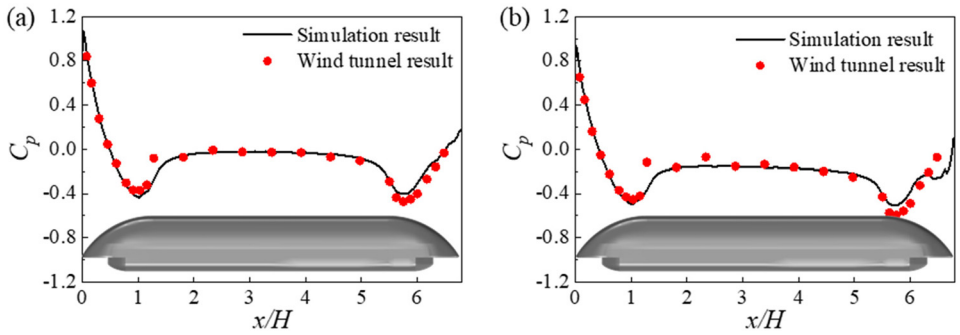

FIG. 6. C_p value of the upper surface along Y = 0 profile of the maglev train obtained by simulation and wind tunnel test: (a) a test speed of 15 m/s and a yaw angle of 0° and (b) a test speed of 15 m/s and a yaw angle of 15°.

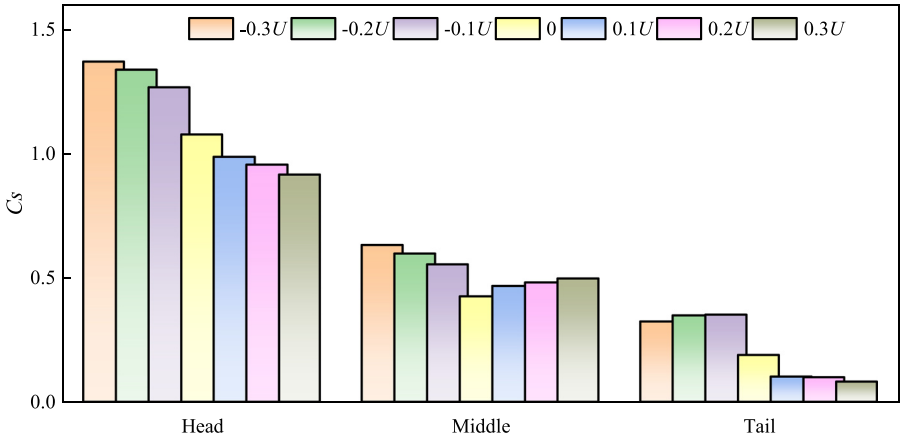

FIG. 7. Aerodynamic lateral force coefficients (*Cs*) acting on each car of the maglev train under various active control strategies.

compared include the original (baseline) case, suction control case ($-0.2U$), and blowing control case ($0.2U$). The fluctuations gradient is quantified by the rate of change of *Cs* values over time. During the simulation period, the peak-to-peak values of the transient *Cs* values are 0.0092% of their respective means for the baseline case, 0.021% for suction control case, and 3.5% for blowing control case. These values indicate that both suction and blowing increase the fluctuation range of the transient lateral force coefficient compared to the baseline from a global statistical perspective. When examining the fluctuations gradient shown in the vertical axis, it is observed that the rate of change of the transient lateral force coefficient occurs in both positive and negative directions around a central value of zero. For the baseline case, suction control case, and blowing control case, the maximum absolute rates of change are 0.06, 0.09, and 10.8, respectively. This observation aligns with the fluctuation ranges indicated on the horizontal axis and demonstrates that suction marginally increases the instability of the transient lateral force's development, while blowing significantly amplifies both the range and intensity of the fluctuations in the value of *Cs*.

In a detailed analysis, the power spectral density (PSD) of the transient lateral forces acting on the head, middle, and tail cars of the maglev train is investigated during the time-discrete process and shown in Fig. 9. The PSD values, processed using the Hanning window function to mitigate spectral leakage, are plotted against the Strouhal number (*St*), which is defined as

$$St = \frac{fH}{U}. \tag{3}$$

To facilitate a clear comparison of the frequency domain characteristics of the transient force coefficients, the data in Figs. 9(a) and

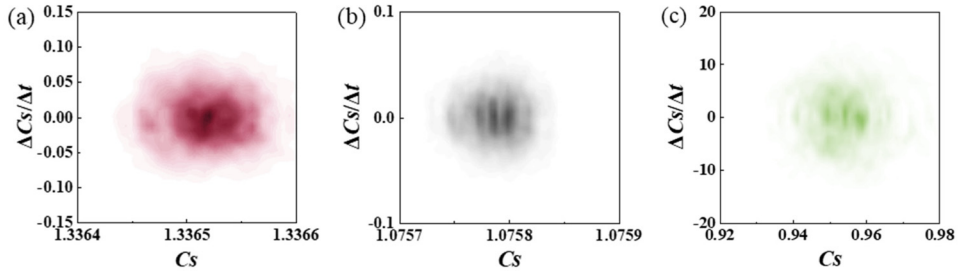

FIG. 8. Distribution and fluctuation of transient aerodynamic lateral force coefficient (*Cs*) of the head car: (a) suction control case ($v_a = -0.2U$), (b) baseline case without any control, and (c) blowing control case ($v_a = 0.2U$).

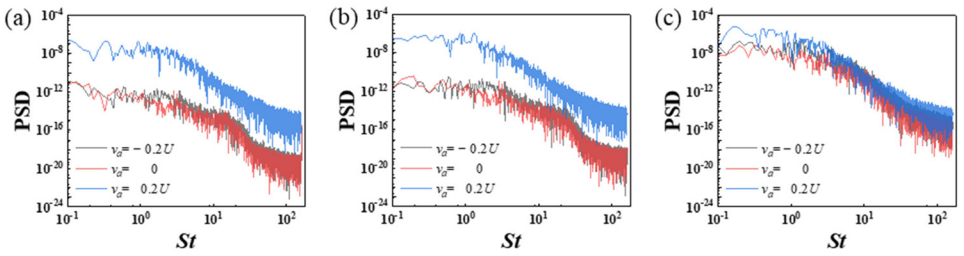

FIG. 9. Power spectral density (PSD) of the transient aerodynamic lateral force coefficient (*Cs*) acting on each car of the maglev train under various active control strategies: (a) head car, (b) middle car, and (c) tail car.

9(b) are presented with transparency. The analysis reveals that the energy content of the transient lateral forces for the head and middle cars is significantly higher under the blowing strategy, with approximately four orders of magnitude greater compared to the baseline case. The suction strategy also exhibits a slight increase in energy content over the baseline, with the difference being within one order of magnitude. The tail car, subject to the largest-scale flow separation and the shedding of major reverse-rotating wake structures, inherently experiences a higher level of instability in its aerodynamic lateral force coefficient compared to the head and middle cars. This results in a naturally high energy level in the transient aerodynamic forces, regardless of the control strategy applied. Nevertheless, the implementation of an active control strategy further escalates the instability of the lateral forces on the trailing car, as evidenced by increased PSD values relative to the baseline condition.

B. Surface flow on the maglev train

In Sec. III A, the significant difference in aerodynamic lateral forces caused by active control strategies can largely be attributed to the different pressures on the windward and leeward sides of the train, which create pressure differential components contributing to the lateral forces. Since the present study applies air slots on the leeward side of the maglev train, with no visible pressure distribution differences expected on the windward side, Fig. 10 illustrates the pressure distribution on the entire leeward side of the train under seven active control strategies (including the baseline case without any active control). Note that the pressure ranges on the tail car, middle car, and tail car are not consistent, so independent color ranges are used for the three cars.

The variations in pressure distribution due to active control strategies are primarily observed in six distinct regions, labeled A–F: Region A is the area where the incoming flow bypasses the streamlined structure of the head car and interacts with the upstream section of the air slot. In this region, suction delays the detachment of the vortex flow that supposed to separate from the head car and entered the wake, causing it to attach closer to this region. This results in a larger negative pressure range and a stronger negative pressure peak. On the other hand, blowing amplifies the flow energy that develops across the roof of the car toward the leeward side, reducing the influence of flow separation on the surface of the car in this region. Consequently, it shows a smaller negative pressure range and positive pressure accumulation formed by the convergence of airflow in the upstream section of the air slot. From the suction strategy [Fig. 10(a)] to the blowing strategy [Fig. 10(g)], the negative pressure in the leeward side region near the streamlined structure of the lead car continuously decreases, and the positive pressure region emerges. This leads to a reduction in the pressure difference between the windward and leeward sides, which is a key factor in the monotonic decrease in the lateral forces on the head car shown in Fig. 7. Another difference on the leeward side of the lead car is observed in region B, which is the area adjacent to the upper and lower sides of the air slot. Apart from the large-scale flow separation near the streamlined structure, slight negative pressure is distributed on the leeward side of cross-sectional segments such as the lead car, as shown in Fig. 10(d). Similarly, suction causes the airflow to stagnate and attach to the train surface, while blowing accelerates the airflow and moves it away from the original position. This creates separate regions of negative or positive pressure in region B, providing an additional push for the monotonic decrease in the lateral forces on the lead car shown in Fig. 7. For the middle car, which initially has a uniform and weak negative pressure distribution on the leeward side, suction and blowing strength the negative pressure below and above the air slot, respectively, as shown in region C, resulting in increased lateral forces on the middle car, corresponding to its behavior in Fig. 7. The air slot directly affects the pressure distribution in the region above it on the trailing car, slightly increasing the level of negative pressure in region D. In the end of the air slot, region E, a phenomenon opposite to that in region A is observed. As the active control strategy shifts from suction to blowing, region E transitions from positive pressure to negative pressure. This is caused by the mixing effect of the two airflows mentioned above. Another change occurs in the streamlined region of the tail car, region F, where the negative pressure is intensified by the suction, resulting in a stronger negative pressure on the leeward side of the streamlined structure. The positive pressure provided by blowing reduces the negative pressure region that should have covered the leeward side of the streamlined structure.

As depicted in Fig. 11, the present study concentrates on three specific longitudinal positions: X1, X2, and X3. These positions correspond to the central points of the air chambers on the lead car, middle car, and trailing car of the maglev train, respectively. The distances from the nose of the lead car to these positions are 4*H*, 9.94*H*, and 15.88*H*.

The influence of the active control strategy is quantitatively evaluated by analyzing the pressure coefficient at positions X1, X2, and X3, as illustrated in Fig. 12. The corresponding pressure coefficients at these locations are depicted in Fig. 11, where the presence of the air slots is indicated by rectangular blocks, where reliable surface pressure data within these blocks is not available. Suction applied through the air slots tends to accumulate negative pressure on the surface directly beneath the chambers. This peak negative pressure correlates with the suction velocity; however, the intensity of this negative pressure diminishes as the distance from the air chamber increases. On the contrary, the application of blowing mitigates the negative pressure under the air slots, nudging the surface pressure toward neutral. The effect of

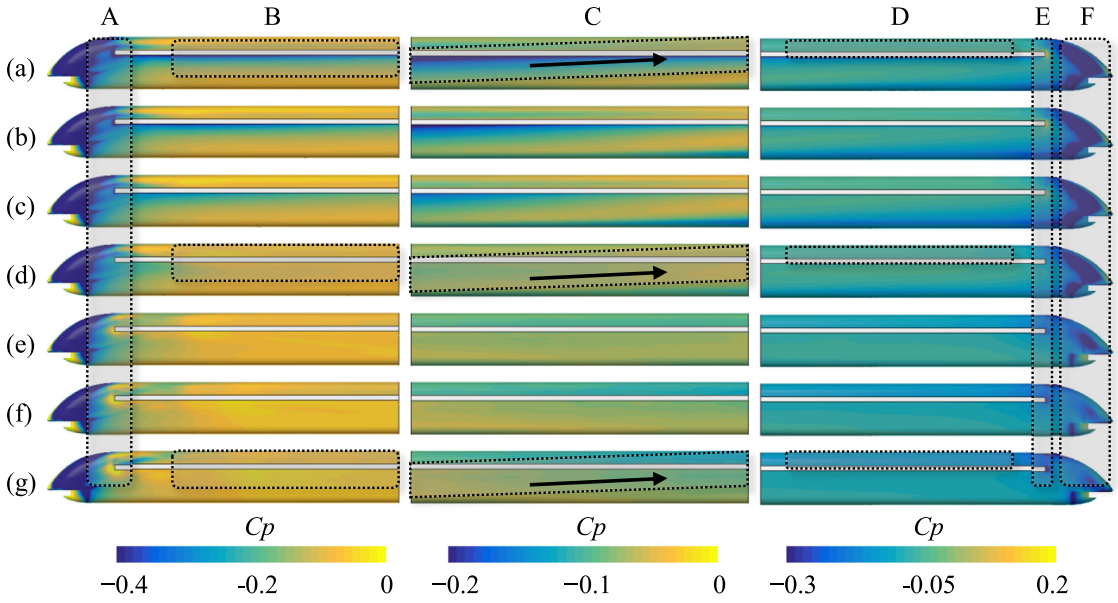

FIG. 10. Pressure distribution on the leeward side surface of the maglev train under various active flow control strategies: (a) $v_a = -0.3U$, (b) $v_a = -0.2U$, (c) $v_a = -0.1U$, (d) baseline case, $v_a = 0$, (e) $v_a = 0.1U$, (f) $v_a = 0.2U$, and (g) $v_a = 0.3U$.

blowing is more pronounced with increased velocity, significantly reducing the negative pressure. Above the air slots, the pressure distribution on the train surface is more intricate due to the dual influence of the incoming flow over the roof and the active airflow emitted from the air slots. Blowing, in particular, tends to reinforce the negative pressure in this region, with the most significant impact observed on the tail car. As can be seen in Figs. 12(d)–12(f), the air slots have less influence on the pressure distribution on the windward side, since these flows occur before being affected by the active flow, especially for the head car, which is the most dangerous in crosswinds. However, a pressure change on the transition of side and roof, brought about by active control, can be detected in the tail car.

C. Spatial flow around the maglev train

Understanding the flow patterns on the leeward side of a maglev train is crucial for grasping the underlying reasons for variations in pressure distribution and aerodynamic lateral forces. Figure 13 showcases these patterns at cross sections X1, X2, and X3 using the line integral convolution of the time-averaged velocity vector. The leeward side of the maglev train is characterized by two prominent swirling structures. The first, a primary vortex, is created by the flow separating from the train's surface at a 15° yaw angle, and its center is indicated by vertical black dashed lines. The second, a secondary vortex, forms as the flow moves past the guideway pedestal and is marked by vertical purple dashed lines. It is important to note that this secondary vortex is a result of the simulated specific scenario including an elevated bridge, and it does not come from the maglev train itself. From Figs. 13(a)–13(f), it is observed that in the baseline and suction cases, the primary vortex maintains a regular shape with a tightly packed rotation. Suction notably slows down the downstream movement of this vortex for the head and middle cars, as shown by the inward shift of the vortex core. This effect is due to the removal of smaller swirling structures in the transition area between the top and leeward side of the maglev train. However, this smaller vortex is absent at the middle position of the tail car [X3, Fig. 13(f)], suggesting that suction does not affect the tail car's primary vortex in the same way. In Figs. 13(g)–13(i), under the blowing strategy, the dominance of the primary vortex is reduced. Instead, it can be seen that a series of alternating smaller flow structures, which are a direct result of the patterns induced by the blowing. Blowing does not push the primary vortex downstream; rather, it lowers its vertical position and spreads out its intensity. This change leads to a reduction in the negative pressure on the leeward side of the train, influencing the aerodynamic forces experienced by the train.

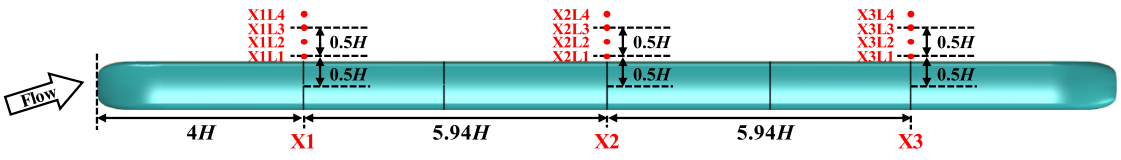

FIG. 11. Location of cross sections and measuring lines in the study.

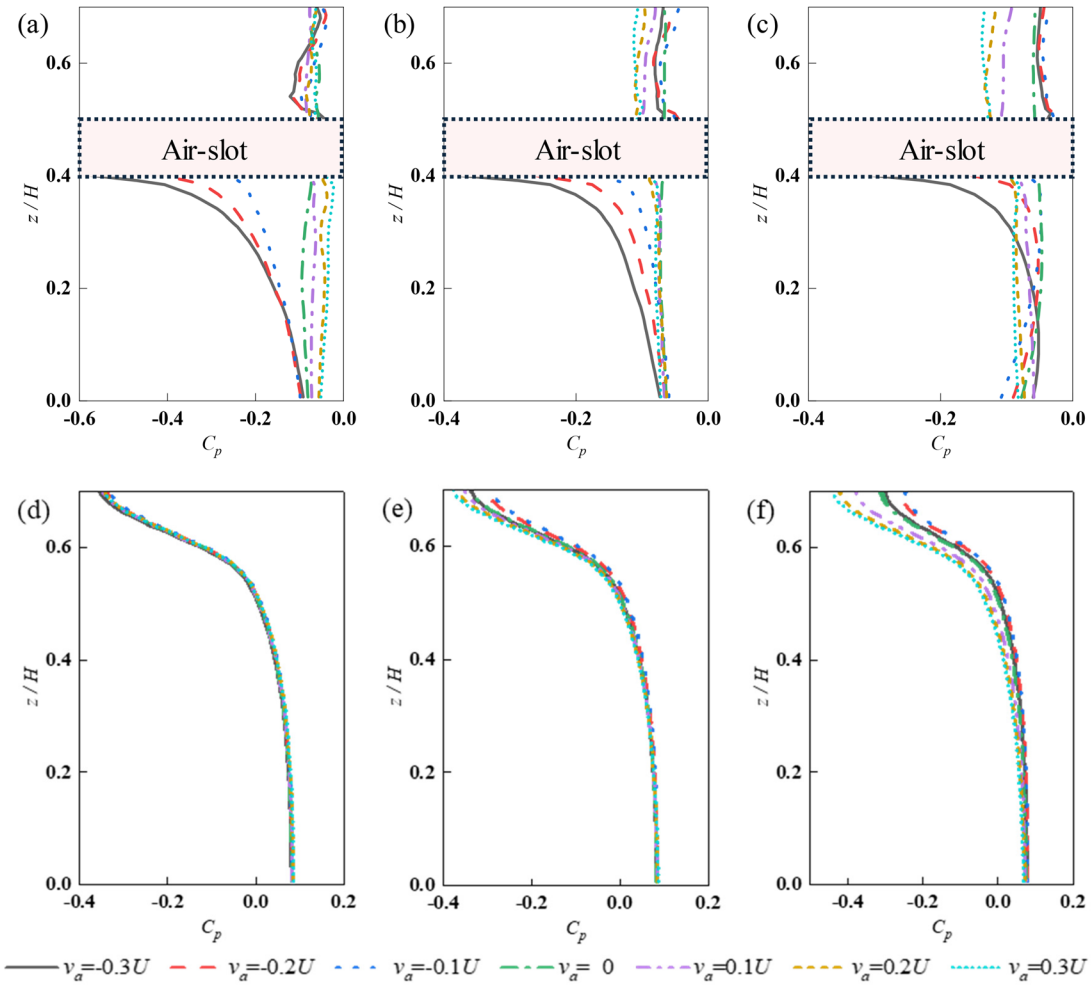

FIG. 12. Pressure distribution on the cross section of the train surface under various active control strategies at the location of (a) X1, leeward side, (b) X2, leeward side, (c) X3, leeward side, (d) X1, windward side, (e) X2, windward side, and (f) X3, windward side.

The non-dimensional turbulent kinetic energy (TKE), which is visualized in Fig. 14, offers additional insights into the flow patterns around the maglev train. TKE is a measure of the energy contained in the turbulent eddies of a flow and is calculated as half the sum of the variances of the fluctuating velocity components in different directions, as calculated below:

$$TKE = \frac{1}{2}\left[\overline{(u')^2} + \overline{(v')^2} + \overline{(w')^2}\right], \tag{4}$$

where u', v', and w' represent the normalized pulsation of velocity along the longitudinal, transverse, and vertical components. Note that to increase the comparability among studies, the non-dimensional TKEs in Fig. 14 are obtained from normalized velocity pulsations, so their values are much smaller than the usual TKE values in $m^2 \cdot s^{-2}$. By examining examine the cross sections from the front to the back of the train (from X1 to X3), it is noticed that the flow continues to evolve, leading to an increase in TKE value. Interestingly, the TKE intensity on the leeward side of the train is significantly reduced when the suction strategy is applied. This decrease in TKE is a result of the inhibitory effect of the suction on the smaller-scale turbulent structures, as illustrated in Figs. 13(a), 13(b), 13(d), and 13(e). On the other hand, when the blowing strategy is in effect, the high TKE values become more concentrated, particularly downstream of the air slot and between the bottom of the air slot and the train roof. By examining Figs. 14(c), 14(f), and 14(i), the blowing strategy eliminates the accumulation of high TKE in the lower region on the leeward side of the tail car. This change is linked to the interaction between the primary and secondary vortices on the leeward side, as the primary vortex expands and occupies the space under the influence of blowing, as depicted in Fig. 13(i).

Figure 15 presents the dimensionless time-averaged lateral velocity (v) profiles along several vertical measurement lines on the leeward side of the maglev train to supplement the understanding of the local and global effects brought by active control strategies. The positions of these measurement lines can be seen in Fig. 11. The direct impact of the active control strategy of the air slot on the lateral velocity can be

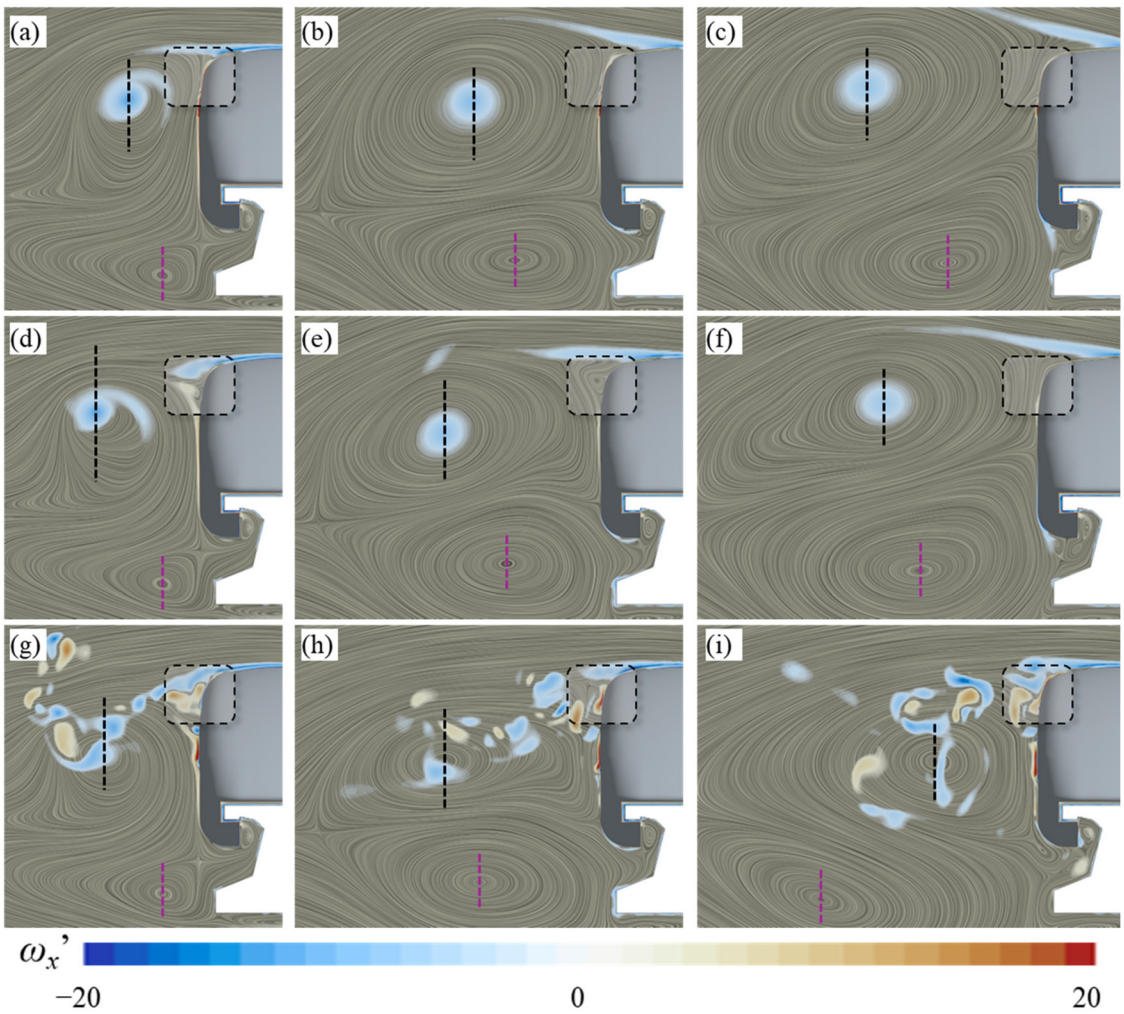

FIG. 13. Velocity vector in the form of line integral convolution and main vorticity distribution downstream the maglev train under various active control strategies: (a) $v_a = -0.2U$, X1, (b) $v_a = -0.2U$, X2, (c) $v_a = -0.2U$, X3, (d) baseline case, $v_a = 0$, X1, (e) baseline case, $v_a = 0$, X2, (f) baseline case, $v_a = 0$, X3, (g) $v_a = 0.2U$, X1, (h) $v_a = 0.2U$, X2, and (i) $v_a = 0.2U$, X3.

observed on the measurement lines X1L1, X2L1, and X3L1, which are adjacent to the air slot. On these measurement lines at the lateral distance from the air slot, the upper region inevitably experiences a chain reaction of the mixed airflow passing through the train roof and the active airflow. On X1L2, X2L2, and X3L2, they are primarily influenced indirectly by the air slot. It can be inferred that the leeward space below the height of the air slot is more significantly influenced by the active control strategy but with a relatively delayed response, and the flow direction is often opposite to the crosswind. On the leeward side above the height of the air slot, the airflow velocity is mostly aligned with the wind direction, and the influence of the control strategy is smaller than that below the air slot. Although the active flow control has a variety of effects on the local velocity at each position, the logic of their differences is clear from the above analysis, and for more detailed differences, see the comprehensive information given in Fig. 15.

D. Energy return assessment

As previously discussed, the implementation of active control strategies plays a pivotal role in modifying the flow patterns on the leeward side of a maglev train, which influences the lateral forces exerted on the train. This manipulation of lateral forces is key to ensuring vehicle safety in the presence of crosswinds. However, the effectiveness of these strategies in altering lateral forces varies depending on the chosen control strategy. In the current research scenario, Fig. 7 illustrates how the aerodynamic lateral forces on each car of the maglev train respond to different suction and blowing velocities under various active control scenarios. The data reveal that increased blowing velocities tend to significantly reduce lateral forces on both the head and tail cars. It is imperative to weigh the benefits of reduced lateral forces against energy consumption to ensure that safety enhancements do not come at an unsustainable energy cost. The benefits of active control in the study were evaluated with reference to the paper. First, the absolute

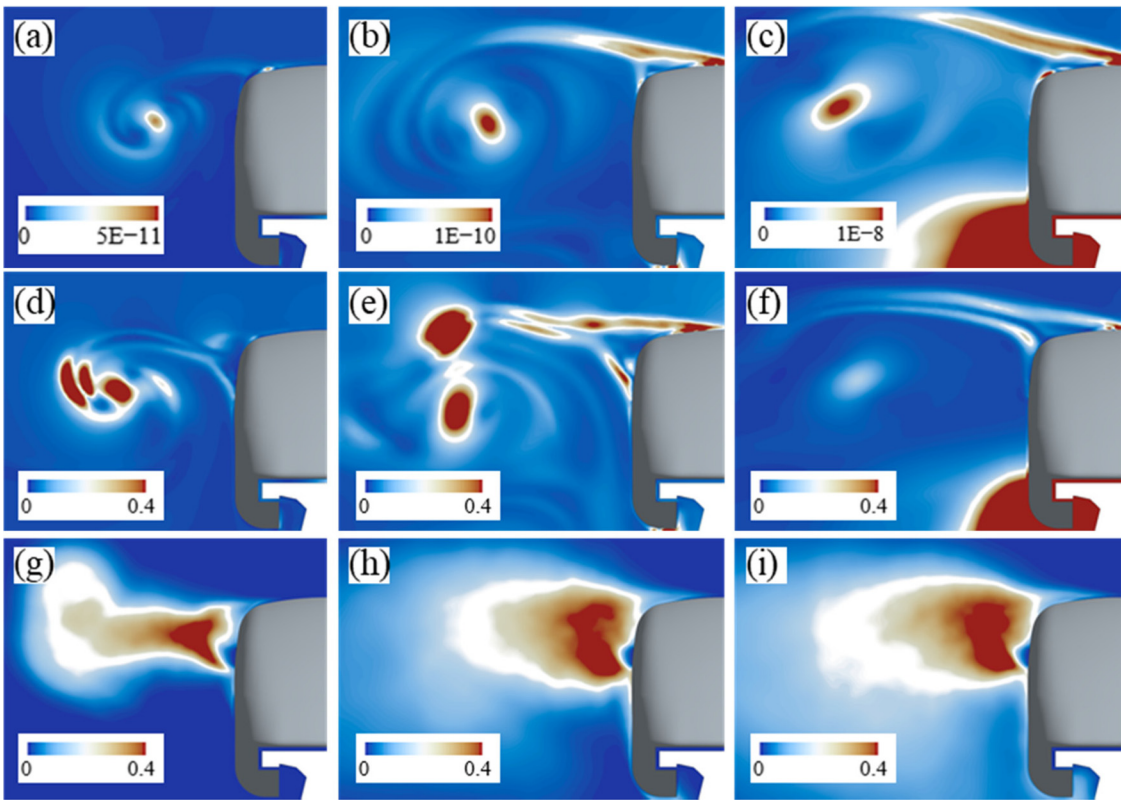

FIG. 14. Distribution of non-dimensional turbulent kinetic energy (*TKE*) downstream the maglev train under various active control strategies: (a) $v_a = -0.2U$, X1, (b) $v_a = -0.2U$, X2, (c) $v_a = -0.2U$, X3, (d) baseline case, $v_a = 0$, X1, (e) baseline case, $v_a = 0$, X2, (f) baseline case, $v_a = 0$, X3, (g) $v_a = 0.2U$, X1, (h) $v_a = 0.2U$, X2, and (i) $v_a = 0.2U$, X3.

change in the aerodynamic lateral force of the independent vehicle ΔF_s is obtained, and it is converted into the power dimension ΔP_s according to the incoming flow velocity; in terms of active control, the power P_a used for active control is obtained based on the blowing or suction speed and the area of air slot, and finally, the energy return coefficient σ is calculated. These definitions are as follows:

$$\Delta F_s = F_{s0} - F_{s1}, \tag{5}$$

$$\Delta P_s = \Delta F_s \cdot U, \tag{6}$$

$$P_a = \frac{1}{2}\rho {v_a}^3 A_a, \tag{7}$$

$$\sigma = \frac{\Delta P_s}{P_a}, \tag{8}$$

where F_{s0} and F_{s1} are the lateral forces acting on each car without and with active control, and A_a is the area of the air slots. To quantify the net power change of various active flow strategies, a value of σ less than 1 indicates that the strategy used will produce an overall energy loss, while a value greater than 1 proves that the current flow control strategy is effective. Effectiveness means achieving higher value at less cost. Table I lists the σ values obtained by using different air blowing strategies for the entire train when operating at different yaw angles studied in this paper. A more visualized heat map is given in Fig. 16. Note that in this evaluation method, the value of σ has no physical meaning, and a value less than 1 only indicates that the current active control strategy is not recommended, regardless of its specific value. Therefore, only a label of <1 is given when displaying the data. When the value of σ is greater than 1, the larger the value, the more it proves the effectiveness of the active control strategy and the high rate of return.

The statistical analysis of the aerodynamic efficiency, as measured by the energy return coefficient, leads to the conclusion that, within the current operational context and given the air slots setup, the use of a blowing strategy does not reduce the lateral force coefficient for the middle car when facing crosswinds. Conversely, employing a suction strategy tends to increase the lateral forces on all cars, compromising the maglev train's stability and safety in crosswind scenarios. However, it is encouraging to note that the blowing strategy significantly mitigates lateral forces on the head car, which are typically the most susceptible to crosswinds. While the analysis shows that the highest aerodynamic efficiency is achieved with a lower flow rate for active control, practical applications must prioritize safety. That is, the head and tail cars obtained the greatest absolute lateral force relief at a blowing velocity of $v_a = 0.3U$, but exhibited the best energy efficiency at $v_a = 0.1U$. Consequently, operators must weigh the absolute aerodynamic "performance" against the "cost-effectiveness" of the control strategies. This balance is crucial and should be carefully considered in light of the specific conditions and requirements of the operating environment.

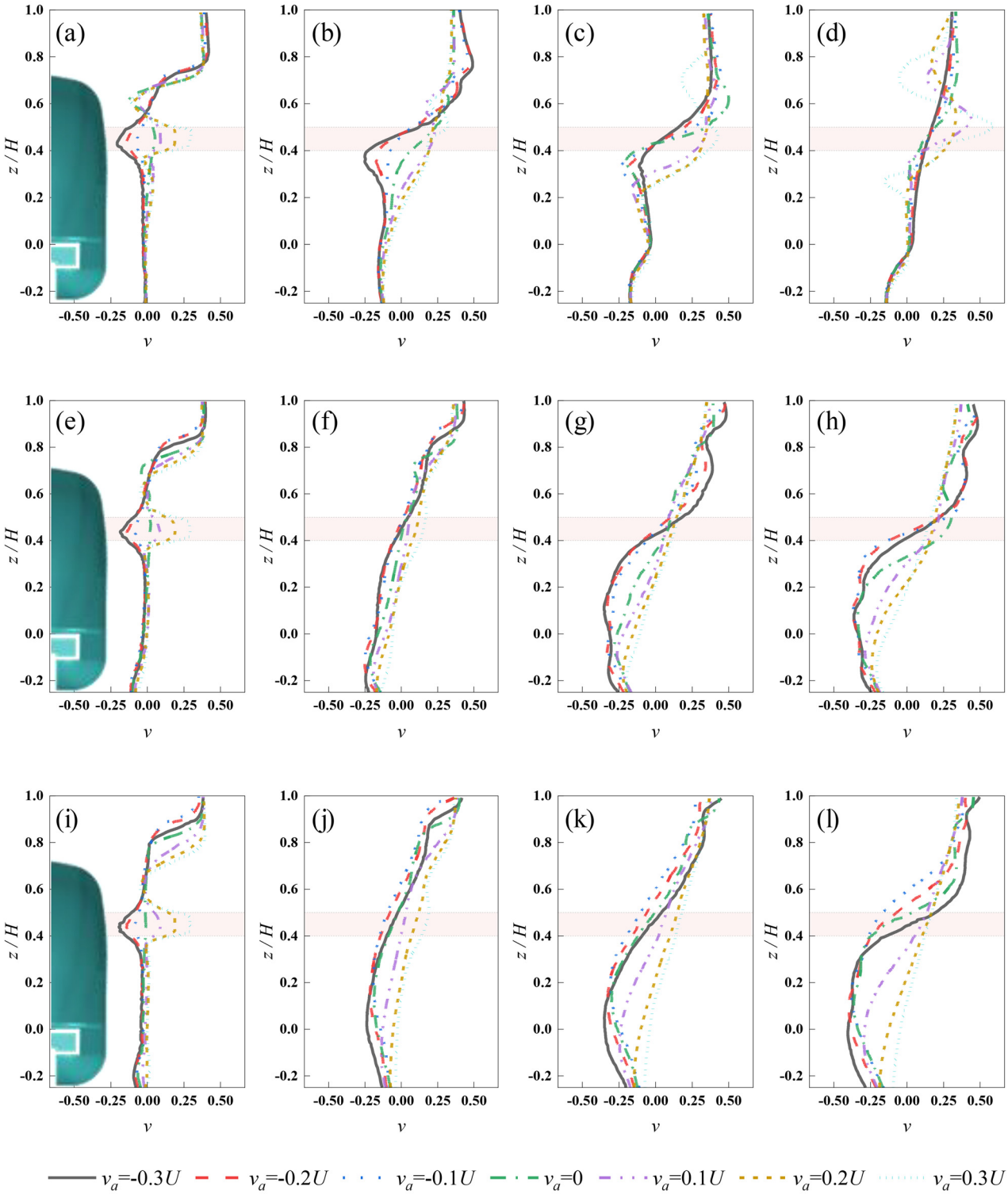

FIG. 15. Dimensionless time-averaged lateral velocity (v) profile downstream the maglev train under various active control strategies: (a) head car, X1L1, (b) head car, X1L2, (c) head car, X1L3, (d) head car, X1L4, (e) middle car, X1L1, (f) middle car, X1L2, (g) middle car, X1L3, (h) middle car, X1L4, (i) tail car, X1L1, (j) tail car, X1L2, (k) tail car, X1L3, and (l) tail car, X1L4.

TABLE I. Energy return coefficient σ under various active control strategies.

Items	The energy return coefficient σ					
v_a	$-0.3U$	$-0.2U$	$-0.1U$	$0.1U$	$0.2U$	$0.3U$
Head	−13.5	−34.8	−236.5	112.0	16.3	7.4
Middle	−24.1	−58.2	−406.4	−133.9	−19.0	−8.4
Tail	−35.6	−122.5	−1154.7	612.5	68.1	28.1
Total	−73.1	−215.5	−1797.5	590.6	65.4	27.1

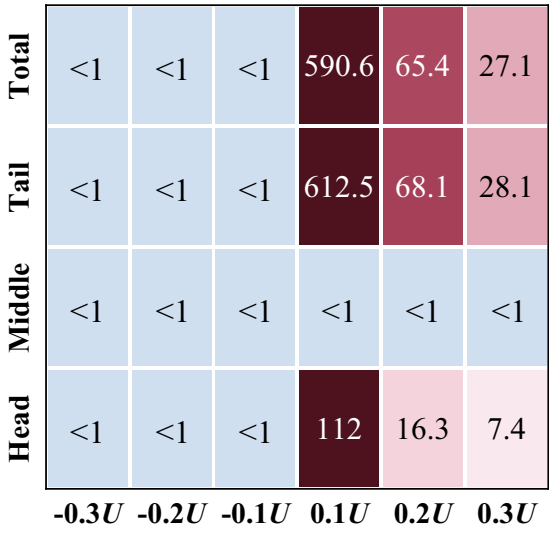

FIG. 16. Heat map of energy return coefficient σ, not showing specific values less than 1.

IV. CONCLUSIONS AND FUTURE WORK

In the present study, the IDDES method based on the SST k–ω turbulence model was used to investigate the effect of active suction and blowing on the leeward side of a maglev train to control its aerodynamic lateral force, multiple control strategies involving blowing and suction velocities were examined, and the main conclusions are summarized as follows:

- Under the current scenario and air slot position, suction increases the time-averaged aerodynamic lateral force coefficients applied to each vehicle, while blowing reduces the lateral forces acting on the head (up to 15%) and tail cars (up to 47%); both active control strategies increase the lateral forces applied to the middle car. Suction and blowing increase fluctuations in the lateral force compared to the baseline, with blowing causing the most significant variation. The energy content of lateral forces is much higher with blowing, especially for the head and middle cars. The tail car naturally experiences high instability due to large-scale flow separation, which is further increased by active control strategies.
- Suction and blowing directly affect the pressure distribution near the air slot region and interact in a complex manner with the primary vortex structure over the roof and secondary vortices below the guideway, indirectly changing the surface flow pattern in more regions: Suction maintains the primary vortex's compact shape and slows its downstream movement, especially for the head and middle cars, but not the tail. Blowing reduces the primary vortex's dominance, creating smaller alternating flow structures, lowering its vertical position, and spreading intensity, which decreases negative pressure and affects aerodynamic forces.
- Suction tends to remove smaller vortex structures in the transition region between the top and the leeward side of the maglev train, inhibiting the downstream motion of the main vortices on the leeward side of the train while substantially weakening the turbulent kinetic energy; blowing reduces the dominance of the main vortices, replacing them with a series of alternating smaller flow structures and concentrating the turbulent kinetic energy near the air slots.
- The application of blowing rather than sucking proved to be an effective means of reducing the risk of operating a maglev train in a crosswind environment. The head and tail cars can obtain the greatest lateral force relief at $v_a = 0.3U$, while the energy return coefficient reach the highest (up to 612.5) at $v_a = 0.1U$. The absolute "aerodynamic performance" of the train and the relative cost-effectiveness of the control strategy must be weighed according to the operating conditions.

Although the application of active flow control on trains is still at an early stage, we have to consider some key issues not yet discussed in this paper to ensure the scientific validity and reliability of these research efforts, such as slot position, slot size, non-constant mass flow rate considerations, and adaptive flow supply for different wind conditions.

ACKNOWLEDGMENTS

This work was supported by the National Natural Science Foundation of China (Grant No. 52202426), grants from the Research Grants Council of the Hong Kong Special Administrative Region, China (Grants No. 15205723 and 15226424), and the Key Program of the National Natural Science Foundation of China (Grant No. 52232013).

AUTHOR DECLARATIONS

Conflict of Interest

The authors have no conflicts to disclose.

Author Contributions

Zi-Jian Guo: Investigation (equal); Methodology (equal); Software (equal); Visualization (equal); Writing – original draft (equal). **Zhan-Hao Guo:** Investigation (supporting); Methodology (supporting); Software (equal); Visualization (supporting); Writing – original draft (supporting). **Zheng-Wei Chen:** Investigation (equal); Resources (equal); Supervision (equal); Software (equal); Validation (equal); Writing – original draft (equal). **Guang-Zhi Zeng:** Data curation (equal); Investigation (supporting); Methodology (equal); Software (supporting); Visualization (supporting). **Jun-Qi Xu:** Data curation (equal); Investigation (equal).

DATA AVAILABILITY

The data that support the findings of this study are available from the corresponding author upon reasonable request.

REFERENCES

[1]M. Kim, J.-H. Jeong, J. Lim, C.-H. Kim, and M. Won, "Design and control of levitation and guidance systems for a semi-high-speed maglev train," J. Electr. Eng. Technol. **12**(1), 117–125 (2017).

[2]J. D. Yau, "Vibration control of maglev vehicles traveling over a flexible guideway," J. Sound Vib. **321**(1), 184–200 (2009).

[3]C. Luo, D. Zhou, G. Chen, S. Krajnovic, and J. Sheridan, "Aerodynamic effects as a maglev train passes through a noise barrier," Flow, Turbul. Combust. **105**(3), 761–785 (2020).

[4]S. Huang, Z. Li, and M. Yang, "Aerodynamics of high-speed maglev trains passing each other in open air," J. Wind Eng. Ind. Aerodyn. **188**, 151–160 (2019).

[5]T. T. Lin, M. Z. Yang, L. Zhang, T. T. Wang, D. R. Liu, Y. Tao, and S. Zhong, "Influence of the suspension gap on the wake characteristics of a 600 km/h superconducting maglev train," Phys. Fluids **36**(2), 026121 (2024).

[6]C. Tan, D. Zhou, G. Chen, J. Sheridan, and S. Krajnovic, "Influences of marshalling length on the flow structure of a maglev train," Int. J. Heat Fluid Flow **85**, 108604 (2020).

[7]Z. X. Sun, M. Y. Wang, L. Y. Wei, F. B. Kong, and G. W. Yang, "Aerodynamic shape optimization of an urban maglev train," Acta Mech. Sin. **37**(6), 954–969 (2021).

[8]G.-Z. Zeng, Z.-W. Li, S. Huang, and Z.-W. Chen, "Aerodynamic characteristics of intercity train running on bridge under wind and rain environment," Alexandria Eng. J. **66**, 873–889 (2023).

[9]H. Wu, X.-H. Zeng, and Y. Yu, "Motion stability of high-speed maglev systems in consideration of aerodynamic effects: A study of a single magnetic suspension system," Acta Mech. Sin. **33**(6), 1084–1094 (2017).

[10]C. Liu, H. Su, C. Wang, and L. Sun, "Vibration control of disturbance gap for maglev vehicle considering stiffness change under unsteady aerodynamic forces," Nonlinear Dyn. **111**(5), 4267–4282 (2023).

[11]S. Krajnović, P. Ringqvist, K. Nakade, and B. Basara, "Large eddy simulation of the flow around a simplified train moving through a crosswind flow," J. Wind Eng. Ind. Aerodyn. **110**, 86–99 (2012).

[12]Z.-W. Chen, Z.-J. Guo, Z.-X. Che, Z.-D. Huang, Y.-Q. Ni, S.-M. Wang, S. Huang, Z.-W. Li, and Q.-X. Wang, "Evaluation of active leeward side air-blowing layout on the lateral aerodynamic performance of high-speed trains in crosswinds environment: Sustainable and safe operation strategy," J. Wind Eng. Ind. Aerodyn. **247**, 105695 (2024).

[13]I. A. Ishak, M. S. Mat Ali, M. F. Mohd Yakub, and S. A. Z. Shaikh Salim, "Effect of crosswinds on aerodynamic characteristics around a generic train model," Int. J. Rail Transp. **7**(1), 23–54 (2019).

[14]Z. Chen, T. Liu, Z. Guo, X. Huo, W. Li, and Y. Xia, "Dynamic behaviors and mitigation measures of a train passing through windbreak transitions from ground to cutting," J. Cent. South Univ. **29**(8), 2675–2689 (2022).

[15]Z. Chen, T. Liu, W. Li, Z. Guo, and Y. Xia, "Aerodynamic performance and dynamic behaviors of a train passing through an elongated hillock region beside a windbreak under crosswinds and corresponding flow mitigation measures," J. Wind Eng. Ind. Aerodyn. **208**, 104434 (2021).

[16]L. Zhang, J. Zhang, T. Li, and Y. Zhang, "A multiobjective aerodynamic optimization design of a high-speed train head under crosswinds," Proc. Inst. Mech. Eng., Part F **232**(3), 895–912 (2018).

[17]S. Yao, D. Guo, Z. Sun, G. Yang, and D. Chen, "Optimization design for aerodynamic elements of high speed trains," Comput. Fluids **95**, 56–73 (2014).

[18]J. Muñoz-Paniagua and J. García, "Aerodynamic surrogate-based optimization of the nose shape of a high-speed train for crosswind and passing-by scenarios," J. Wind Eng. Ind. Aerodyn. **184**, 139–152 (2019).

[19]Z. Chen, T. Liu, Z. Jiang, Z. Guo, and J. Zhang, "Comparative analysis of the effect of different nose lengths on train aerodynamic performance under crosswind," J. Fluids Struct. **78**, 69–85 (2018).

[20]Z. Guo, T. Liu, Z. Chen, Y. Xia, W. Li, and L. Li, "Aerodynamic influences of bogie's geometric complexity on high-speed trains under crosswind," J. Wind Eng. Ind. Aerodyn. **196**, 104053 (2020).

[21]W. Shang, G. Gao, X. Miao, J. Zhang, and J. Wang, "Impact of bogie fairing configuration on the aerodynamic performance of high-speed train under crosswind," Mech. Based Des. Struct. Mach. **52**(9), 6209–6224 (2023).

[22]Z. Jiang, T. Liu, H. Gu, and Z. Guo, "A numerical study of aerodynamic characteristics of a high-speed train with different rail models under crosswind," Proc. Inst. Mech. Eng., Part F **235**(7), 840–853 (2021).

[23]B. Xu, X. Chen, T. Liu, Z. Chen, W. Li, Y. Xia, X. Huo, H. Gao, and H. Liu, "On the anti-rolling performance of a train using a vortex generator array," Eng. Appl. Comput. Fluid Mech. **17**(1), 2275614 (2023).

[24]H. Gu, T. Liu, Z. Jiang, and Z. Guo, "Experimental and simulation research on the aerodynamic effect on a train with a wind barrier in different lengths," J. Wind Eng. Ind. Aerodyn. **214**, 104644 (2021).

[25]S. A. Hashmi, H. Hemida, and D. Soper, "Wind tunnel testing on a train model subjected to crosswinds with different windbreak walls," J. Wind Eng. Ind. Aerodyn. **195**, 104013 (2019).

[26]G. Tomasini, E. Brambilla, and S. Cii, "Safety to crosswind of railway vehicles in presence of wind barriers: Numerical-experimental approach," in *Advances in Dynamics of Vehicles on Roads and Tracks*, edited by M. Klomp, F. Bruzelius, J. Nielsen, and A. Hillemyr (Springer International Publishing, Cham, 2020), pp. 312–316.

[27]Y. Xia, T. Liu, X. Su, Z. Jiang, Z. Chen, and Z. Guo, "Aerodynamic influences of typical windbreak wall types on a high-speed train under crosswinds," J. Wind Eng. Ind. Aerodyn. **231**, 105203 (2022).

[28]X. Wang, X. Hu, J. Wang, L. Wang, H. Li, Z. Deng, and W. Zhang, "Safety analysis of high temperature superconducting maglev train considering the aerodynamic loads under crosswinds," Proc. Inst. Mech. Eng., Part C **237**(10), 2279–2290 (2023).

[29]Z. Li, X. Wang, Y. Ding, J. Wang, P. Liu, and Z. Deng, "Study on the dynamics characteristics of HTS maglev train considering the aerodynamic loads under crosswinds," Sustainability **15**(23), 16511 (2023).

[30]F. Zhu, J. Xie, D. Lv, G. Xu, H. Yao, and J. Niu, "Transient aerodynamic behavior of a high-speed Maglev train in plate braking under crosswind," Phys. Fluids **36**(3), 035133 (2024).

[31]S. Ho, H. Nassef, N. Pornsinsirirak, Y.-C. Tai, and C.-M. Ho, "Unsteady aerodynamics and flow control for flapping wing flyers," Prog. Aerosp. Sci. **39**(8), 635–681 (2003).

[32]S. Scott Collis, R. D. Joslin, A. Seifert, and V. Theofilis, "Issues in active flow control: Theory, control, simulation, and experiment," Prog. Aerosp. Sci. **40**(4), 237–289 (2004).

[33]Z.-W. Chen, G.-Z. Zeng, Y.-Q. Ni, T.-H. Liu, J.-Q. Niu, and H.-D. Yao, "Reducing the aerodynamic drag of high-speed trains by air blowing from the nose part: Effect of blowing speed," J. Wind Eng. Ind. Aerodyn. **238**, 105429 (2023).

[34]Z.-X. Che, S. Huang, Z.-W. Li, and Z.-W. Chen, "Aerodynamic drag reduction of high-speed maglev train based on air blowing/suction," J. Wind Eng. Ind. Aerodyn. **233**, 105321 (2023).

[35]K. Jin, L. Zhang, X. Li, L. Li, J. Chen, J. Wang, and J. Niu, "Effect of characteristic parameters of air-bleeding/blowing interface on tunnel pressure waves in streamlined regions of high-speed trains: A numerical simulation study," Sustainable Cities Soc. **102**, 105222 (2024).

[36]Z.-W. Chen, Y.-Q. Ni, Y.-W. Wang, S.-M. Wang, and T.-H. Liu, "Mitigating crosswind effect on high-speed trains by active blowing method: A comparative study," Eng. Appl. Comput. Fluid Mech. **16**(1), 1064–1081 (2022).

[37]Z.-J. Guo, Z.-W. Chen, Z.-X. Che, A. Bordbar, and Y.-Q. Ni, "Using leeward air-blowing to alleviate the aerodynamic lateral impact of trains at diverse yaw angles," Phys. Fluids **36**(4), 045121 (2024).

[38]J. Zhang, Y. Ding, F. Wang, N. Xiang, A. Xu, Z. Chen, and M. Tang, "Comparison of aerodynamic performance of trains running on bridges under crosswinds using various motion modes," Phys. Fluids **35**(12), 125125 (2023).

[39]L. Li, T. Liu, Z. Guo, W. Li, and Y. Xia, "On the effect of rail-end slope in train aerodynamics under crosswind," Veh. Syst. Dyn. **60**, 1888–1908 (2021).

[40]E. Deng, H. Yue, X.-Y. Liu, and Y.-Q. Ni, "Aerodynamic impact of wind-sand flow on moving trains in tunnel-embankment transition section: From field testing to CFD modeling," Eng. Appl. Comput. Fluid Mech. **17**, 2279993 (2023).

[41]J. Niu, D. Zhou, and X. Liang, "Experimental research on the aerodynamic characteristics of a high-speed train under different turbulence conditions," Exp. Therm. Fluid Sci. **80**, 117–125 (2017).
[42]R.-D. Xue, X.-H. Xiong, X.-B. Li, and G. Chen, "Influence of turbulent incoming flow on aerodynamic behaviors of train at 90° yaw angle," Phys. Fluids **35**(1), 015121 (2023).
[43]X.-S. Huo, T.-H. Liu, Z.-W. Chen, W.-H. Li, J.-Q. Niu, and H.-R. Gao, "Aerodynamic characteristics of double-connected train groups composed of different kinds of high-speed trains under crosswinds: A comparison study," Alexandria Eng. J. **64**, 465–481 (2023).
[44]Z. Guo, T. Liu, Y. Xia, and Z. Liu, "Aerodynamic influence of the clearance under the cowcatcher of a high-speed train," J. Wind Eng. Ind. Aerodyn. **220**, 104844 (2022).
[45]Z. Guo, T. Liu, Z. Liu, X. Chen, and W. Li, "An IDDES study on a train suffering a crosswind with angles of attack on a bridge," J. Wind Eng. Ind. Aerodyn. **217**, 104735 (2021).